Electronic Supplementary Information (ESI) for

Exploring orientationally aligned anisotropic large spin molecules with unusual long-distance intermolecular ferromagnetic interactions†

Takuo Minato,[a] Yusuke Ohata,[a] Kazuyuki Ishii,[b] Kazuya Yamaguchi,[a] Noritaka Mizuno[a]

and Kosuke Suzuki * [a,c]

[a] Department of Applied Chemistry, School of Engineering, The University of Tokyo, 7-3-1 Hongo, Bunkyo-ku, Tokyo 113-8656, Japan. E-mail: ksuzuki@appchem.t.u-tokyo.ac.jp

[b] Institute of Industrial Science, The University of Tokyo, 4-6-1 Komaba, Meguro-ku, Tokyo 153-8505, Japan

[c] Precursory Research for Embryonic Science and Technology (PRESTO), Japan Science and Technology Agency (JST), 4-1-8 Honcho, Kawaguchi, Saitama 332-0012, Japan

Table S1. BVS values of oxygen, silicon, vanadium, manganese, and tungsten atoms of **I**.

O1	2.142	O24	1.981
O2	2.061	O25	1.975
O3	0.808	O26	1.881
O4	0.855	O27	1.867
O5	0.776	O28	1.950
O6	0.823	O29	1.899
O7	1.783	O30	1.895
O8	1.708	O31	1.882
O9	1.736	O32	1.685
O10	1.847	O33	1.613
O11	1.803	O34	1.618
O12	1.653	Si1	3.858
O13	2.011	V1	2.955
O14	2.093	W1	6.182
O15	1.990	W2	6.169
O16	2.132	W3	5.910
O17	2.044	W4	6.030
O18	2.123	W5	6.015
O19	2.258	W6	5.976
O20	1.859	W7	5.885
O21	1.849	W8	5.744
O22	1.964	W9	5.832
O23	1.992		

Table S2. BVS values of oxygen, silicon, vanadium, manganese, and tungsten atoms of **II-a**.

O1	2.050	O33	1.750	O65	1.778
O2	2.041	O34	1.897	O66	1.887
O3	1.876	O35	1.834	O67	1.759
O4	1.827	O36	1.877	O68	1.944
O5	1.811	O37	2.035	O1H	1.160
O6	1.861	O38	2.045	O2H	1.160
O7	1.731	O39	1.864	Si1	3.987
O8	1.698	O40	1.830	Si2	3.978
O9	1.726	O41	1.676	V1	2.929
O10	1.689	O42	1.952	Mn1	2.976
O11	1.712	O43	1.698	Mn2	3.001
O12	1.712	O44	2.041	Mn3	2.974
O13	1.981	O45	1.717	Mn4	2.976
O14	2.051	O46	1.981	W1	6.102
O15	1.918	O47	1.685	W2	6.114
O16	1.967	O48	2.024	W3	6.039
O17	2.000	O49	1.726	W4	5.986
O18	2.051	O50	1.934	W5	5.951
O19	1.911	O51	1.759	W6	5.983
O20	2.005	O52	1.971	W7	6.073
O21	2.009	O53	2.006	W8	6.073
O22	2.036	O54	1.933	W9	6.008
O23	1.952	O55	2.002	W10	6.042
O24	2.008	O56	2.053	W11	6.017
O25	2.019	O57	1.989	W12	6.066
O26	1.978	O58	1.980	W13	5.982
O27	2.009	O59	2.023	W14	6.030
O28	1.970	O60	1.969	W15	6.019
O29	1.712	O61	2.021	W16	6.021
O30	1.922	O62	1.954	W17	6.079
O31	1.694	O63	1.662	W18	6.019
O32	1.978	O64	1.941		

Table S3. BVS values of oxygen, silicon, vanadium, manganese, and tungsten atoms of **II-b**.

O1	2.053	O33	1.783	O65	1.937
O2	2.021	O34	1.649	O66	1.722
O3	1.882	O35	2.057	O67	1.722
O4	1.876	O36	2.061	O68	1.708
O5	1.851	O37	1.846	O1H	1.163
O6	1.898	O38	1.815	O2H	1.157
O7	1.759	O39	1.844	Si1	3.997
O8	1.722	O40	1.918	Si2	3.967
O9	1.754	O41	1.680	V1	2.985
O10	1.694	O42	1.745	Mn1	2.997
O11	1.698	O43	1.745	Mn2	3.003
O12	1.745	O44	1.703	Mn3	2.976
O13	2.022	O45	1.703	Mn4	2.922
O14	2.047	O46	1.754	W1	6.121
O15	1.979	O47	2.003	W2	6.170
O16	1.995	O48	2.059	W3	6.108
O17	1.990	O49	1.968	W4	6.037
O18	2.098	O50	2.014	W5	6.010
O19	1.940	O51	2.013	W6	6.113
O20	2.031	O52	2.045	W7	5.990
O21	2.029	O53	1.957	W8	6.065
O22	1.974	O54	2.024	W9	6.081
O23	2.029	O55	2.019	W10	6.109
O24	2.046	O56	1.952	W11	6.163
O25	2.001	O57	2.046	W12	6.040
O26	2.019	O58	2.029	W13	6.063
O27	2.021	O59	1.984	W14	6.062
O28	1.956	O60	2.024	W15	6.063
O29	1.888	O61	2.033	W16	6.094
O30	1.943	O62	1.966	W17	6.078
O31	1.931	O63	1.947	W18	6.147
O32	1.708	O64	1.961		

Table S4. Selected bond lengths (Å) in **II-a** and **II-b**. The Jahn-Teller axes are marked in bold in the table and are represented as green bonds in the ball and stick representation of {VMn_4} core.

II-a		**II-b**	
V1–O19	**2.072**	**V1–O19**	**2.071**
V1–O1	1.981	V1–O1	1.964
V1–O2	1.985	V1–O2	1.970
V1–O54	**2.077**	**V1–O53**	**2.081**
V1–O37	1.967	V1–O35	1.972
V1–O38	1.983	V1–O36	1.968
Mn1–O20	**2.162**	**Mn1–O20**	**2.162**
Mn1–O1H	1.958	Mn1–O1H	1.965
Mn1–O3	1.906	Mn1–O3	1.885
Mn1–O4	1.898	Mn1–O4	1.892
Mn1–O37	1.897	Mn1–O36	1.909
Mn2–O21	**2.153**	**Mn2–O21**	**2.150**
Mn2–O1H	1.964	Mn2–O1H	1.956
Mn2–O5	1.890	Mn2–O5	1.892
Mn2–O6	1.901	Mn2–O6	1.895
Mn2–O38	1.897	Mn2–O35	1.909
Mn3–O55	**2.147**	**Mn3–O55**	**2.155**
Mn3–O2H	1.968	Mn3–O2H	1.966
Mn3–O2	1.904	Mn3–O1	1.906
Mn3–O39	1.902	Mn3–O39	1.904
Mn3–O40	1.898	Mn3–O40	1.887
Mn4–O53	**2.148**	**Mn4–O54**	**2.138**
Mn4–O2H	1.956	Mn4–O2H	1.959
Mn4–O1	1.910	Mn4–O2	1.910
Mn4–O35	1.894	Mn4–O37	1.909
Mn4–O36	1.908	Mn4–O38	1.924

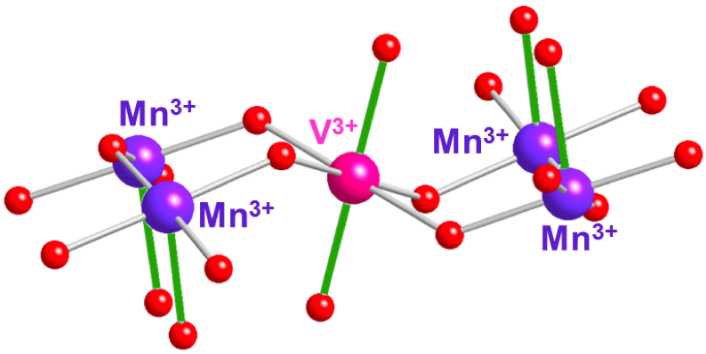

Table S5. Average bond lengths (Å) and bond angles (°) in the $\{VMn_4\}$ cluster in **II-a** and **II-b**.

	Bond lengths (Å)	
	II-a	**II-b**
V–O(–Mn)	1.979	1.969
V–O(–Si)	2.075	2.076
Mn–O(–V)	1.902	1.909
Mn–O(–Mn)	1.962	1.962
Mn–O(–Si)	2.153	2.151
V···Mn	3.507	3.501
Mn···Mn	3.538	3.530
	Bond angles (°)	
	II-a	**II-b**
∠V–O–Mn	129.29	129.14
∠Mn–O–Mn	128.77	128.23

Table S6. Relationships between molecular orientations and magnetic properties of **II-a**, **II-b**, and **III**.

	II-a	**II-b**	**III**
Number of molecular orientation in the crystal	1	2	1
Spin ground state	9	9	11/2
Intermolecular ferromagnetic interaction	yes	no	no

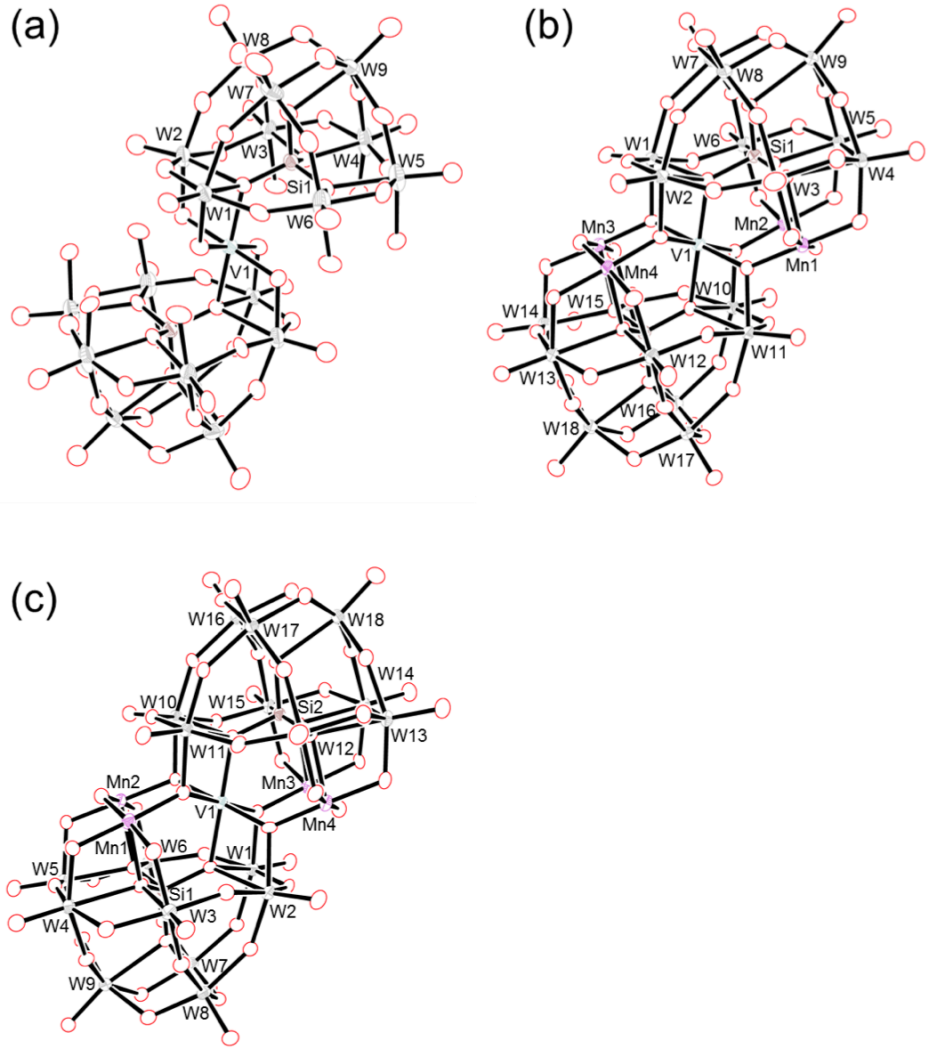

Fig. S1 ORTEP representations of the anion part of (a) **I**, (b) **II-a**, and (c) **II-b** with thermal ellipsoids drawn at the 50% probability level.

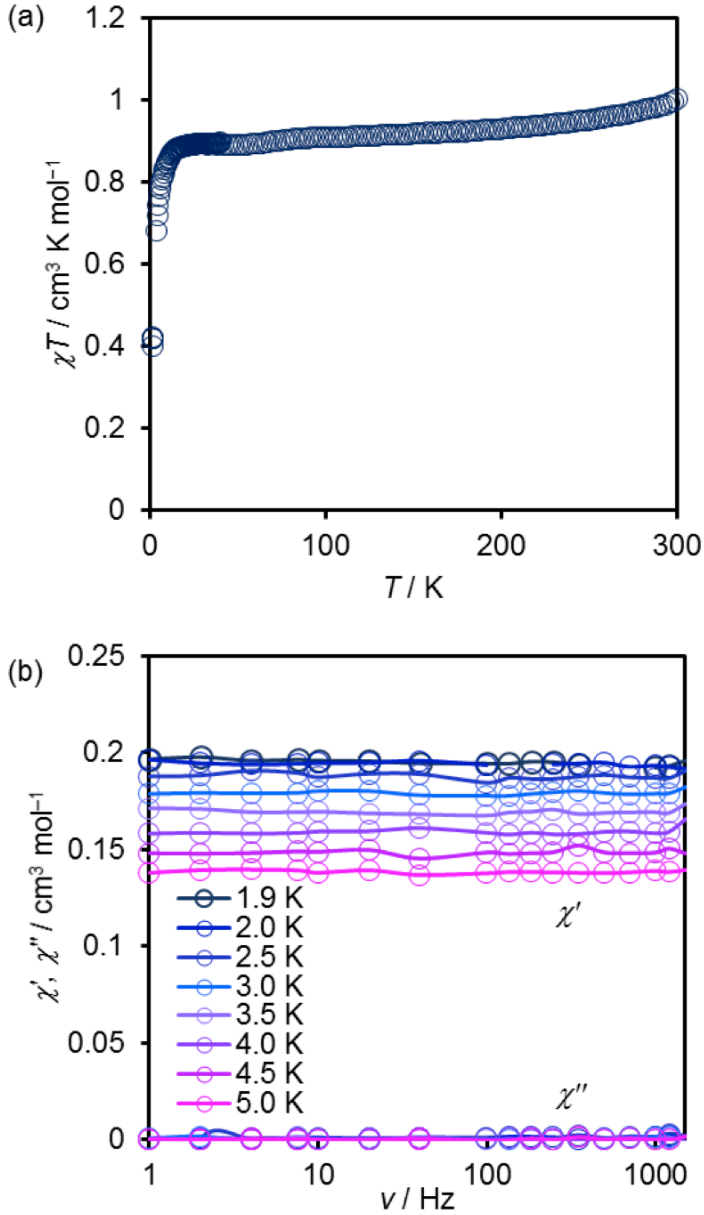

Fig. S2 (a) Temperature dependence of χT for **I** under the applied dc magnetic field of 0.1 T and (b) frequency dependence of the ac magnetic susceptibilities of χ' and χ'' for **I** under the applied dc magnetic field of 0.1 T.

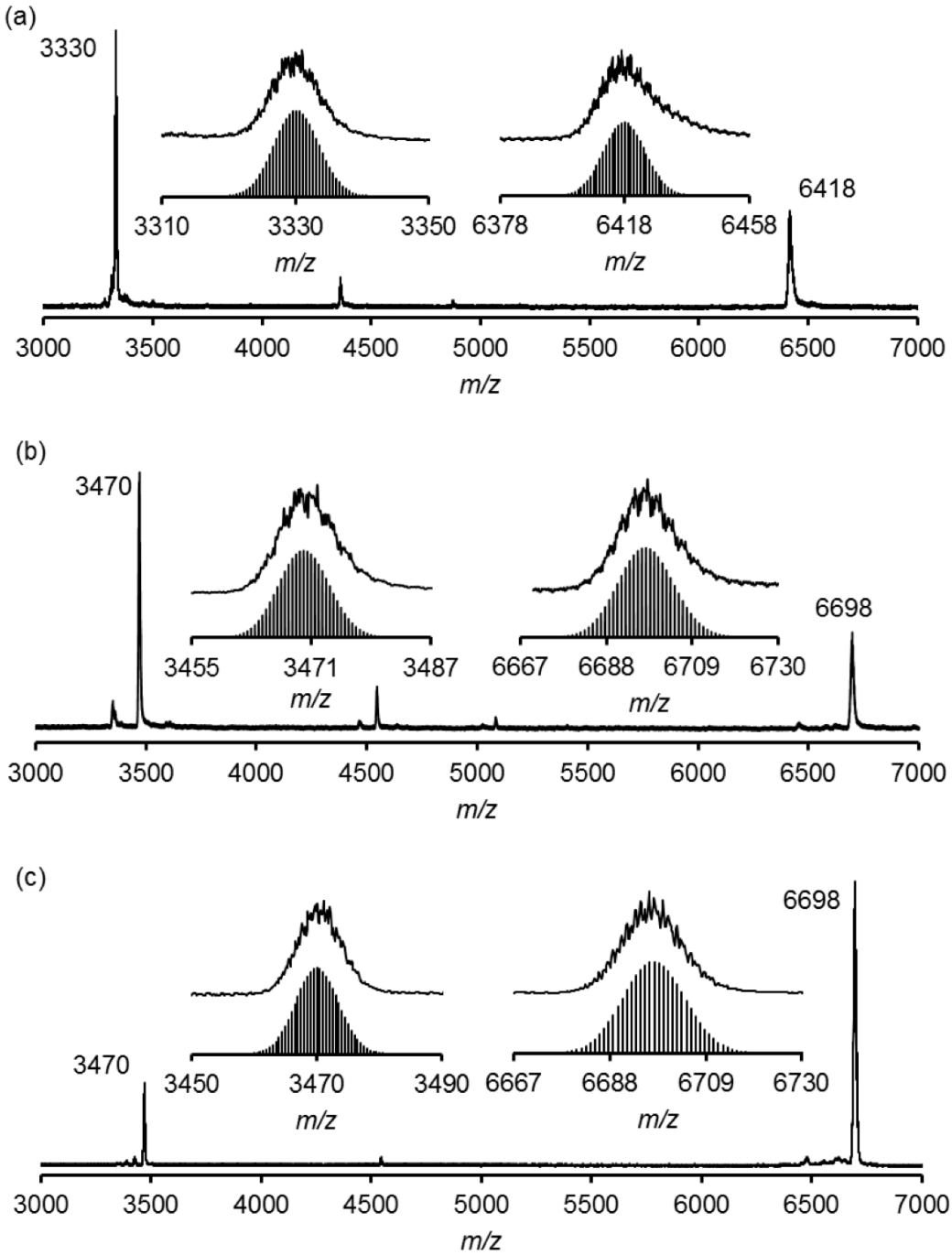

Fig. S3 Positive-ion CSI mass spectra of the polycrystalline sample of (a) **I**, (b) **II-a**, and (c) **II-b** in 1,2-dichloroethane. Insets: (a) spectra in the range of *m/z* 3310–3350 and 6378–6458 and simulated patterns for $[TBA_9H_6Si_2W_{18}O_{66}V]^{2+}$ (*m/z* 3330.2) and $[TBA_8H_6Si_2W_{18}O_{66}V]^{+}$ (*m/z* 6418.0), (b) spectra in the range of *m/z* 3455–3487 and 6667–6730 and simulated patterns for $[TBA_9H_2Si_2W_{18}O_{70}VMn_4]^{2+}$ (*m/z* 3470.1) and $[TBA_8H_2Si_2W_{18}O_{70}VMn_4]^{+}$ (*m/z* 6697.7), (c) spectra in the range of *m/z* 3450–3490 and 6667–6730 and simulated patterns for $[TBA_9H_2Si_2W_{18}O_{70}VMn_4]^{2+}$ (*m/z* 3470.1) and $[TBA_8H_2Si_2W_{18}O_{70}VMn_4]^{+}$ (*m/z* 6697.7).

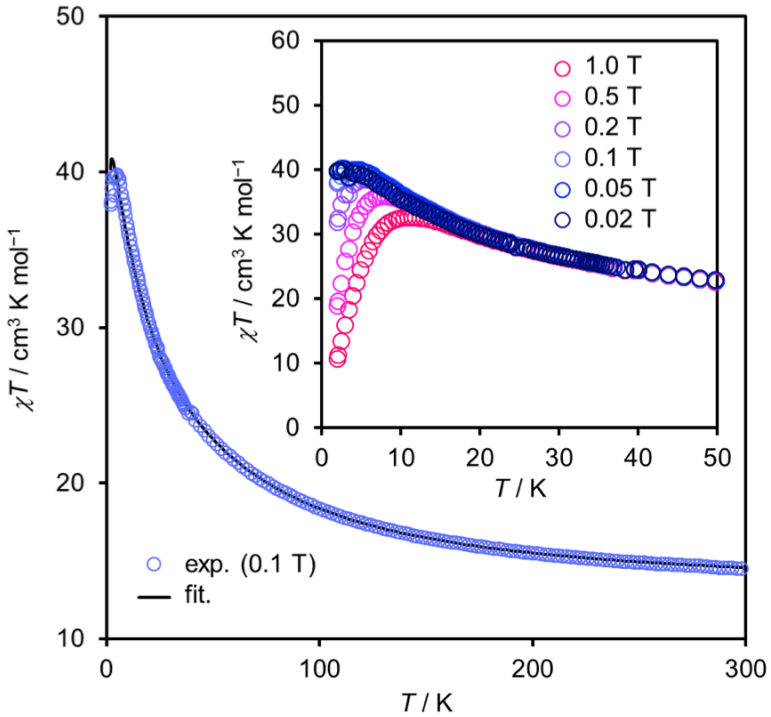

Fig. S4 Temperature dependences of χT for **II-b** under the applied dc field of 0.1 T. Inset: Temperature dependences of χT for **II-b** under various external dc magnetic fields. The solid line represents the best fit adopting the Heisenberg–Dirac–Van Vleck Hamiltonian.

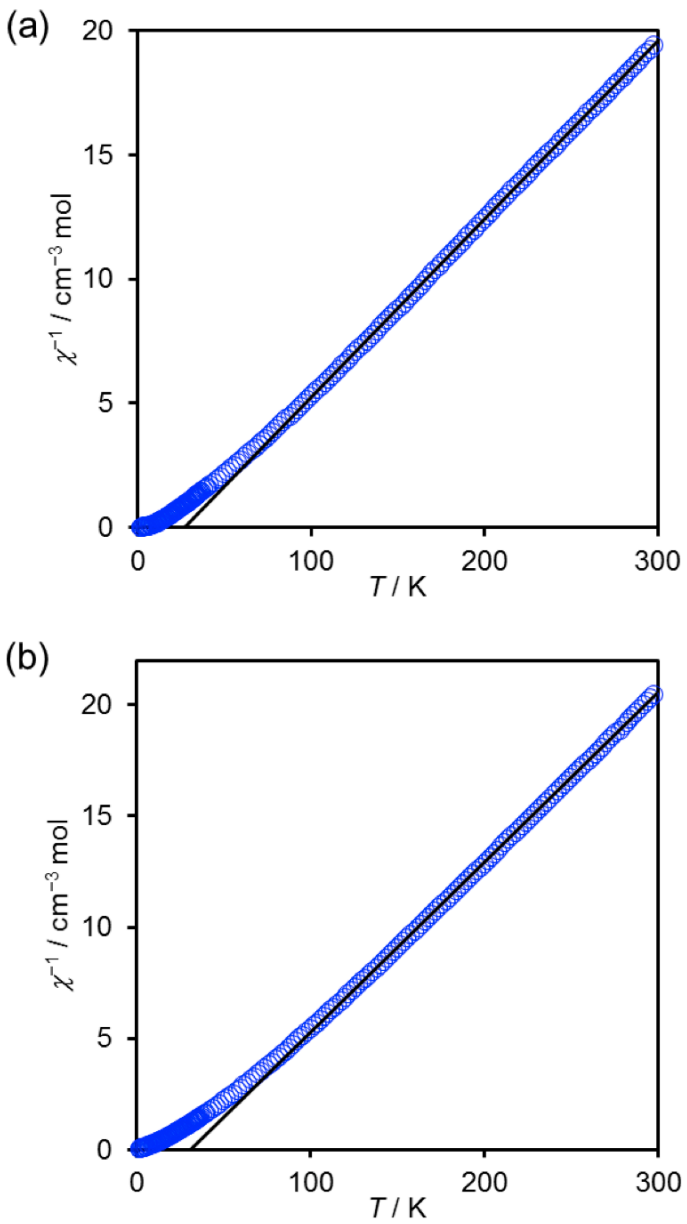

Fig. S5 Temperature dependences of the inverse magnetic susceptibilities (χ^{-1}) for (a) **II-a** and (b) **II-b**. Solid lines represent the best fits for the Curie–Weiss law ($\chi = C/(T - \theta)$) in a temperature range of 100–300 K with (a) C = 13.97 cm^3 K mol^{-1}, θ = 26.74 K and (b) C = 13.09 cm^3 K mol^{-1}, θ = 30.77 K.

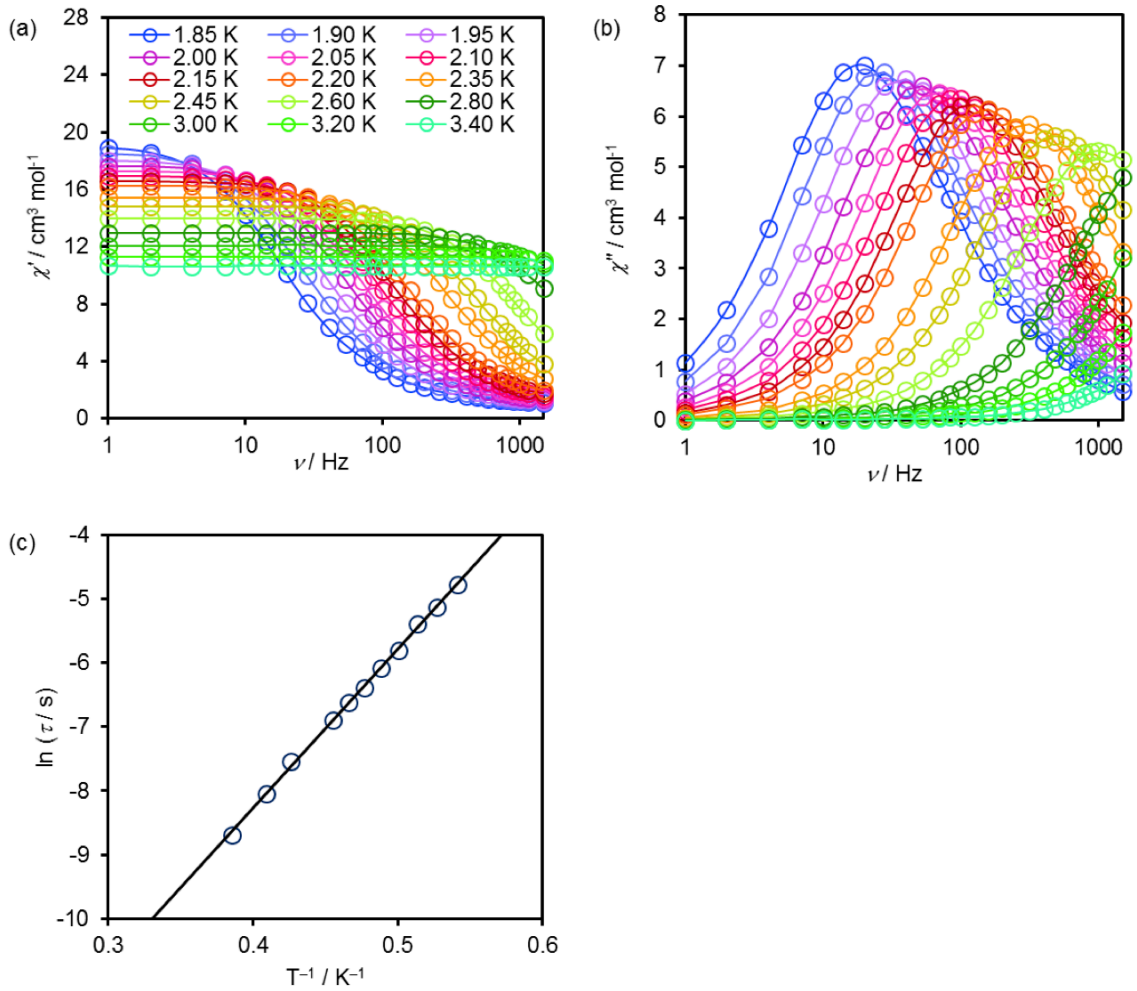

Fig. S6 Frequency dependence of the ac magnetic susceptibilities of a) χ' and b) χ'' for **II-a** under the zero dc magnetic field. c) Plots of relaxation time (τ) versus T^{-1} for **II-a**. The solid line represents the best fit with the Arrhenius law ($\ln\tau$ ($\tau = \tau_0\exp(U_{eff}/k_BT)$) vs T^{-1}) at thermally activated regime, showing the energy barriers for magnetization reversal (U_{eff}) of 26.7 K.

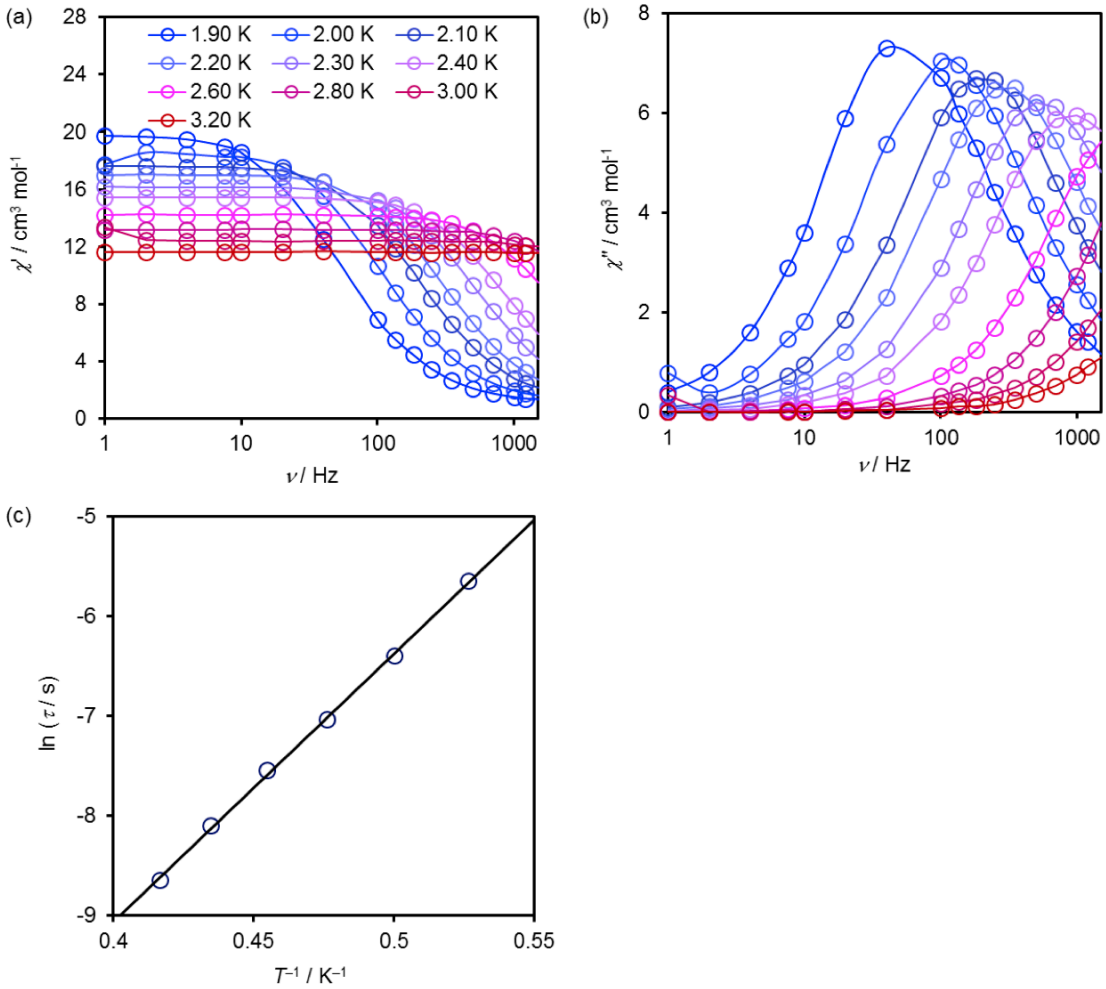

Fig. S7 Frequency dependence of the ac magnetic susceptibilities of a) χ' and b) χ'' for **II-b** under the zero dc magnetic field. c) Plots of relaxation time (τ) versus T^{-1} for **II-b**. The solid line represents the best fit with the Arrhenius law ($\ln\tau$ ($\tau = \tau_0\exp(U_{eff}/k_BT)$) vs T^{-1}) at thermally activated regime, showing the energy barriers for magnetization reversal (U_{eff}) of 26.9 K.

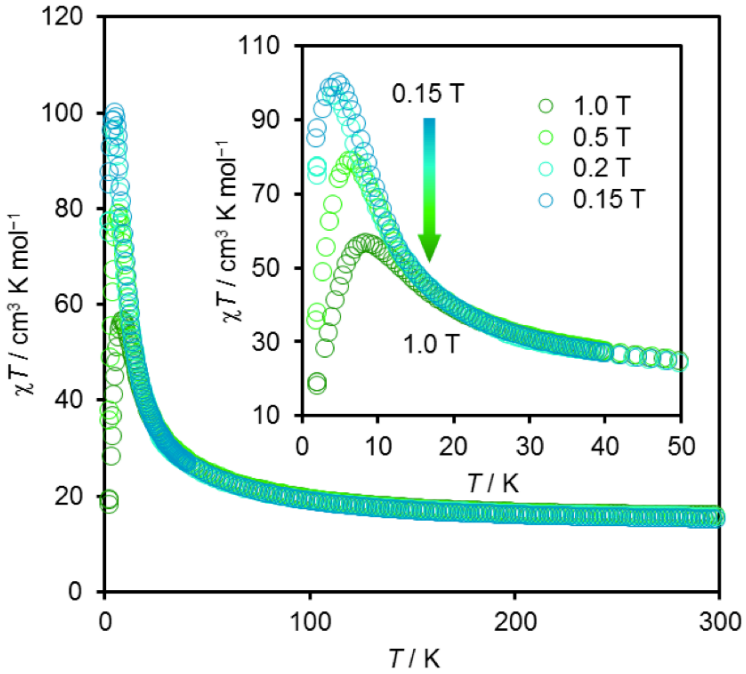

Fig. S8 Temperature dependences of χT for **II-a** under various external dc magnetic fields. Inset: Enlarged view of temperature dependences of χT.

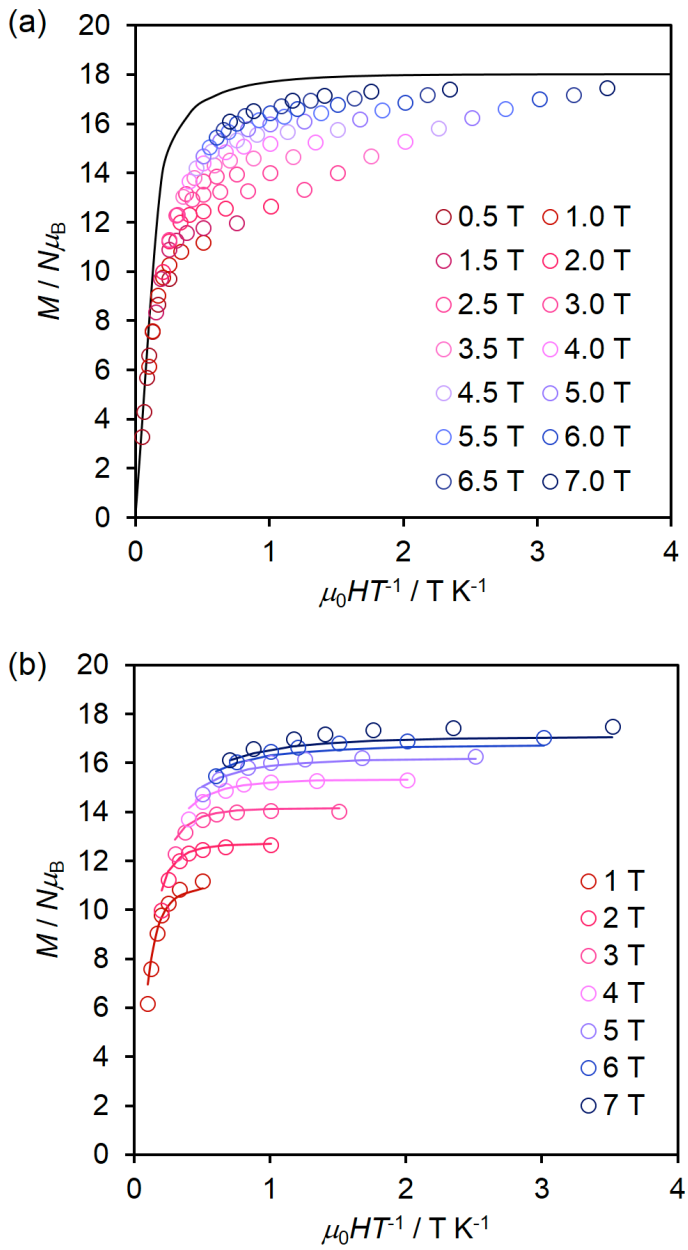

Fig. S9 Low temperature magnetization data for **II-b**. (a) The black solid line represents the Brillouin function with $S_T = 9$. (b) The colored solid lines represent the best fits adopting the following Hamiltonian: $\boldsymbol{H} = D(S_z^2 - S(S+1))/3 + E(S_x^2 - S_y^2) + \mu_B g\mathbf{SH}$. The best fits parameters, which were obtained by the PHI program, were as follows: $D = -0.29$ cm^{-1}, $|E| = 1.53 \times 10^{-5}$, and $g = 1.99$, supporting the large uniaxial magnetic anisotropy ($D < 0$, $|E/D| \sim 10^{-5}$).

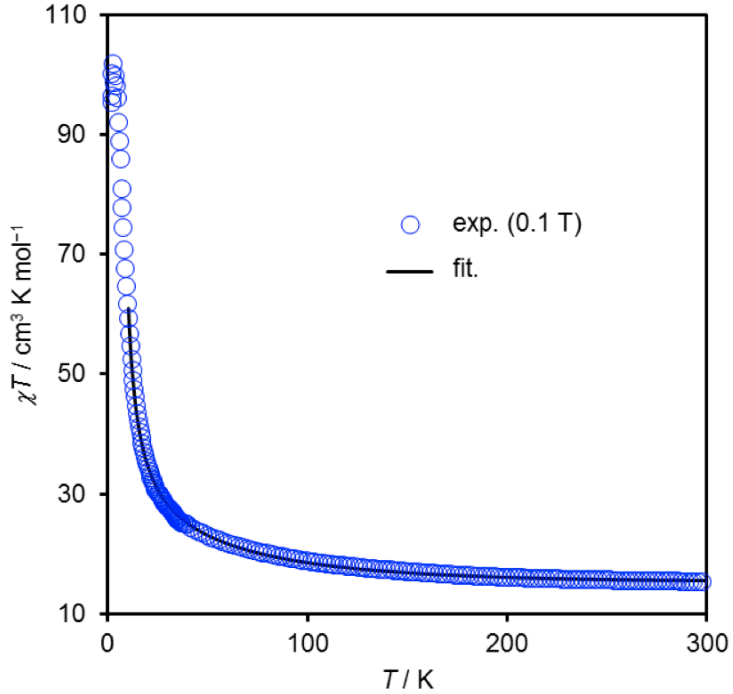

Fig. S10 Temperature dependence of χT for **II-a** under the applied dc field of 0.1 T. The solid line represents the best fit adopting the Heisenberg–Dirac–Van Vleck Hamiltonian.

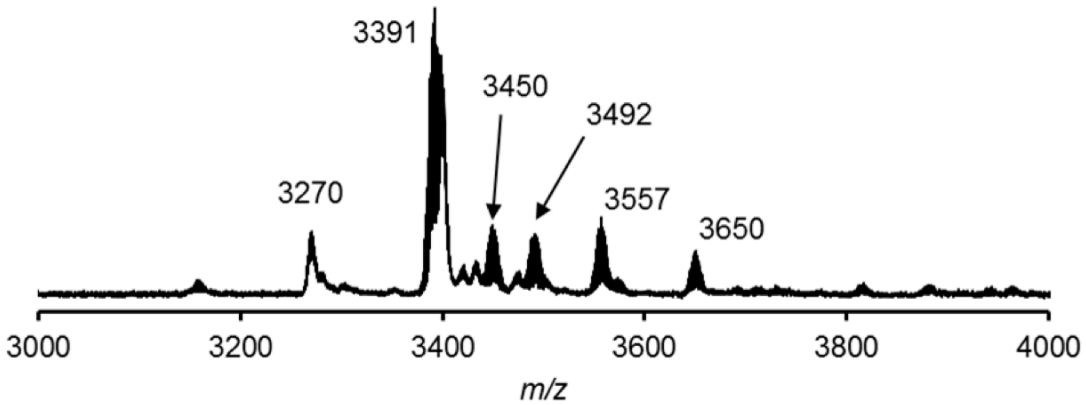

Fig. S11 Positive-ion CSI mass spectra of the synthetic solution of V-containing POM under the air. Signal sets at *m/z* 3270, 3391, 3492, and 3557 were assignable to $[TBA_9HSi_2W_{18}O_{62}]^{2+}$ (*m/z* 3270.2), $[TBA_{10}Si_2W_{18}O_{62}]^{2+}$ (*m/z* 3391.0), $[TBA_5H_2SiW_9O_{34}V^{4+}]^{+}$ (*m/z* 3491.9), and $[TBA_5SiW_9O_{35}V^{4+}{}_2]^{+}$ (*m/z* 3556.8). Signal sets at *m/z* 3450 and 3650 could not be assigned.

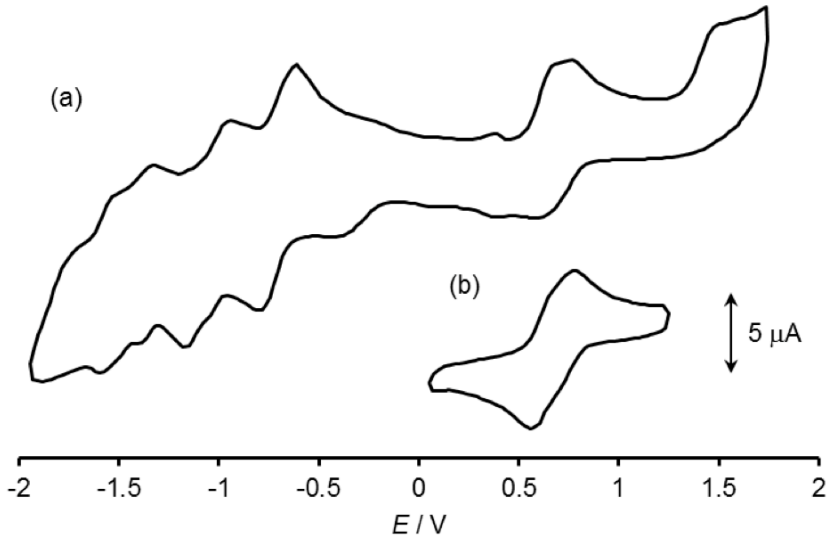

Fig. S12 Cyclic voltammogram of **I** in acetonitrile in the range of (a) –1.95–1.75 V and (b) 0.05–1.25 V (0.5 mM **I**, 100 mM $TBAClO_4$).

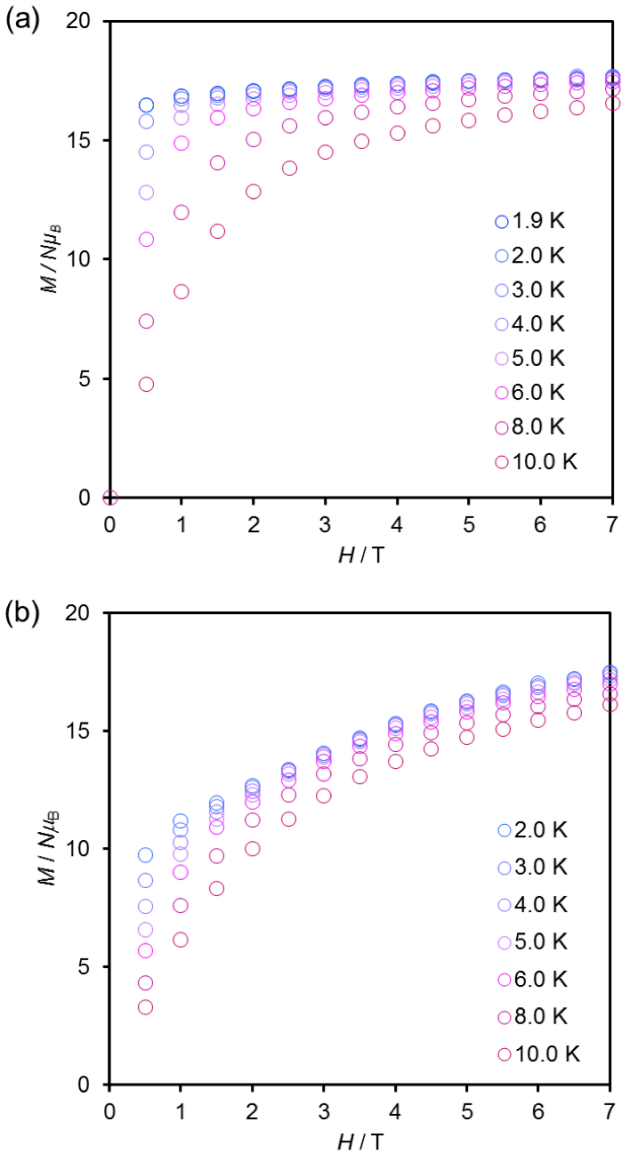

Fig. S13 Low temperature magnetization data for (a) **II-a** and (b) **II-b**.